RIS-assisted SWIPT Network for Internet of Everything under the Electromagnetics-based Communication Model

Ruoyan Ma, Jie Tang, *Senior Member, IEEE,* Xiu Yin Zhang, *Fellow, IEEE,* Kai-Kit Wong, *Fellow, IEEE,* Jonathon A. Chambers, *Fellow, IEEE,*

***Abstract*—In the Internet of Everything (IoE) scenarios, the extensive deployment of devices may result in more stringent power and communication needs. Within this context, we utilize the reconfigurable intelligent surface (RIS) to support the simultaneous wireless information and power transfer (SWIPT) system, whereby the stable transmission of energy and information services can be guaranteed. Specifically, we construct the system model through electromagnetics (EM), which is based on the scattering-parameter (S-parameter) analysis, for revealing the crucial factors of the practical hardware. Relying on the model, the energy-efficient (EE) maximization problem constrained to the quality of services (QoS) is proposed for the users with the framework of co-located receiver (Rx). However, the problem is more intractable due to the introduced channel model. To resolve it, we propose an effective optimization scheme. First, the Neuman series approximation method is adopted to deconstruct the EM transfer model. Then the reformed problem, which includes the variables (i.e., the PS ratio, the active beamformer, and the reflection-coefficient matrix), can be addressed through the strategy of alternative optimization (AO). Further, the inner convex approximation (INCA) scheme and Dinkelbach's algorithm are applied to tackle each sub-problem. In the numerical simulation, we demonstrate that the array configuration can influence not only the hardware properties of RIS but also the EE performance of the whole system. What's more, the proposed scheme performs better for the tightly-coupled RIS owing to the awareness of the mutual-coupling (MC) effect.**

***Index Terms*—S-parameter analysis, mutual coupling, reconfigurable intelligent surface, simultaneous wireless information and power transfer, and energy efficiency.**

I. Introduction

THE idea of the Internet of Everything (IoE) expands on the principles of the Internet of Things (IoT) by embracing a larger network of interconnected devices, entities, and individuals. Through the extensive network of sensors, actuators, and processers, the autonomous decisions of ordinary objects could be feasible [1]. Nevertheless, due to uncountable access devices, it brings a tough issue to power massive nodes simultaneously [2]. During deployment, the work of manual inspection and maintenance may be burdensome, particularly for conventional techniques (i.e., battery supply and cable supply). Therefore, innovating the energy-supply approach is urgent to promote the wider usage of IoE.

Using the existing electromagnetic (EM) energy is more flexible and feasible for IoE-based scenarios, as data are continually being sent between devices via EM waves. Therefore, simultaneous wireless information and power transfer (SWIPT) technology, which incorporates wireless information transfer (WIT) and wireless power transfer (WPT), can be implemented to achieve the dual goals of IoT devices [3]. Regardless of the scenarios, the forms of SWIPT users can be divided into two categories, the colocated and the separated. Particularly, their main difference revolves around the necessity for both information demodulation (ID) and energy harvesting (EH) to be satisfied simultaneously [4]. When these needs are required simultaneously, namely colocated form, the splitting schemes should be deployed to divide the two streams. Additionally, many conditions might influence the choice of the splitting techniques, such as power splitting (PS), time switching (TS), and polarization separation [5].

Despite having a broad application prospect, the SWIPT system has strict criteria for channel quality. In particular, the harvested power typically ranges under milliwatts (mW), even when line of sight (LoS) channels exist [6]. As a result, the situation of inadequate harvested power is even worse under conditions without LoS transfer. Fortunately, a reconfigurable intelligent surface (RIS), which offers channel controllability, has been demonstrated as a potential solution for guaranteeing the stable transmission of SWIPT. [4]. Typically, RIS is an array with numerous state-controlled elements. In detail, their reflection coefficients can be regulated by the varactor diodes or PIN diodes [7]. This is where RIS's functionality originates. During the system design, the factors (e.g., element design and array configuration) that influence the reflection performance of RIS must be carefully considered [8]. This means the modeling of RIS should be reasonable. Particularly, utilizing typical approaches of the EM analysis is feasible. In the next subsection, the efforts related to EM-based models and RIS-assisted-SWIPT networks are presented.

A. Related Works

1) End-to-end communication system based on EM theory: Since the multiple-input multiple-output (MIMO) network was

Manuscript received October 23, 2023; revised December 11, 2023;. This work was supported by the National Natural Science Foundation of China under Grant No. 62222105.

Ruoyan Ma, Jie Tang *(Corresponding author)*, Xiu Yin Zhang are with the School of Electronic and Information Engineering, South China University of Technology, Guangzhou 510641, China (e-mail: eeruoyan_ma@mail.scut.edu.cn; eejtang@scut.edu.cn; eexyz@scut.edu.cn).

Kai-Kit Wong is with the Department of Electronic and Electrical Engineering, University College London, WClE 6BT London, U.K (e-mail: kai-kit.wong@ucl.ac.uk).

Jonathon A. Chambers is with the School of Engineering, University of Leicester, Leicester LE1 7RH, U.K (e-mail:jonathon.chambers@leicester.ac.uk).

proposed, the physical characteristics of the array designs have been recognized as the non-negligible components of the system design. There are several representative instances. Particularly, the MIMO transfer model, including the mutually-coupled array, matching network, and amplifier, is introduced for exposing the impacts of hardware on capacity [9]. Specifically, the EM analysis relying on scattering parameters (S-parameters) is adopted. The results demonstrate that the capacity is distinct between the ideal (i.e., no hardware features) and the non-ideal situations. Moreover, the system models constructed on frequency-dependent impedances are proposed to analyze the effects of physical antennas [10]. The simulation further illustrates that the achievable rate is directly influenced by the distinct array configurations (parallel or co-linear). Besides, the practical performance evaluation, considering non-ideal factors caused by mutual coupling (MC) of the transceiver, is conducted in a holographic MIMO system [11]. It shows that compact arrays distort not only the patterns and radiation efficiency but also the channel capacity.

2) EM modeling of RIS: Compared to the array in a MIMO system, the RIS may incorporate more elements to achieve better performance owing to its passivity. Furthermore, the RIS units have more flexible configurations and control strategies. These facts explain that it is impractical to oversimplify the RIS model during the construction of the system [12]. Indeed, several works have considered these non-negligible factors in the theoretical research. Particularly, the amplitudes and phase shifts of the reflection coefficients are remodeled from the EM perspective [13]. As a result, the position and orientation of RIS are taken into account as important factors during the system optimization. Besides, the impedance-matrix-based approach, which depends on the EM calculation of the dipole configuration, is introduced to define the RIS-based communication system [14]. The results indicate that the MC effect of RIS cannot be disregarded. Additionally, the modified RIS model, taking into account the carrier frequency, characteristics of the incident wave, and the MC effect, is presented from the EM perspective [15]. Particularly, it reveals that the amplitudes and phase shifts are coupled and may bring huge challenges for optimization. Following the similar consideration, the method-of-moments (MoM) based approach is adopted to model the arbitrary-configuration RIS [16]. The numerical results show that the offered modeling method outperforms the normally-utilized simplified model.

3) RIS-aided communication system: Numerous studies regarding RIS-integrated communication systems have been conducted for a while. Typically, the scenarios include heterogeneous networks [17], backscatter communication [18], and emergency communication [19]. Specifically, RIS provides more critical performance benefits by enhancing the channel quality of SWIPT. In detail, the related works are distinct in the network architectures (i.e., MIMO [20], [21] and MISO [4]), structures of the user (i.e., colocated [4] and separated [20]), and objective formulations (i.e., sum-rate maximization [20], total transmitting-power minimization [21] and harvested-power maximization [22]). Regardless of the manner in which RIS-assisted-SWIPT systems are developed, the rectifying circuit is the critical hardware that needs to be analyzed carefully. Particularly, its prominent indicator is the rectifying efficiency, which represents the conversion capability from the radio-frequency (RF) power to the direct-current (DC) power and is impacted by many factors (i.e., characteristics of rectifier diode and waveforms). With the consideration of these physical properties, the fitting model [4] and analytical model based on waveform design [23] are introduced in the network.

B. Motivation and Contributions

With the idea of expressing the physical features, this paper aims to construct an end-to-end communication model based on EM theory. According to [24], the proposed model is further extended and the physical properties are presented explicitly. Specifically, this model serves as a bridge between theoretical analysis and hardware design. Then we propose an effective solution scheme for a hardware-feature awareness problem based on the model. The main contributions are summarized as the following items:

- Unlike the impedance-transfer model [14], the S-parameter-based theory is employed to construct the entire system model, which is not constrained by the particular configuration of the antenna and thus is more general. With this model, the crucial physical characteristics of the main EM devices and their load circuits are presented. Additionally, the S-parameter-based system is easier for further extensions, which include but are not limited to the power amplifier and the matching circuit.
- With the introduction of the end-to-end model, the EE maximization problem becomes more challenging under the RIS-assisted-SWIPT network scenario. Particularly, the inverse form of the channel causes the problem cannot be solved directly. To further simplify it, we present the Neuman series approximation. Then, the problem can be transformed into successive approximated problems and the iteration-based method can be applied to resolve them.
- Although the problem can be simplified through the above strategy, the approximated problems of each iteration are still non-convex issues, which include several coupled variables. Therefore, we utilize the alternative optimization (AO) approach to separate them. During the solution procedure of each subproblem, the approach of the inner convex approximation (INCA) and Dinkelbach's algorithm are adopted to convert it into a convex form.
- In the numerical simulation, we analyze the relationship between EE indicators and QoS requirements. The convergence behaviors are also presented to show the effectiveness of the proposed optimization scheme. To illustrate the practicality of the model, we design an RIS and import its S-parameter into the model. The impact of its physical characteristics on the EE performance is shown. Particularly, the results demonstrate that the configurations of RIS, especially the accompanying MC effect, have a direct impact on the system performance.

C. Organization and Notations

The paper is organized as follows. Section II presents the EM-based end-to-end system model, which is extended from the S-parameter theory. Through the model, the EE maximization problem of the network is proposed. In Section III, an algorithm scheme with the Neuman series approximation is utilized to address the problem. Section IV shows the rationality of the model and the effectiveness of the optimization strategy. What is more, several performance comparisons of the network are carried out through the actual EM entities.

Matrices and vectors are denoted as boldface letters $\mathbf{a}$ and $\mathbf{A}$, while scalars are presented by a. Besides, $|a|$ denotes the norm of a. $\|\mathbf{a}\|_2$ represents the Euclidean norm of the vector $\mathbf{a}$. Furthermore, the spectral norm, the Hermitian conjugate transpose, the transpose, the trace and the rank of the matrix $\mathbf{A}$ can be denoted as $\|\mathbf{A}\|$, $\mathbf{A}^H$, $\mathbf{A}^T$, $\mathrm{Tr}(\mathbf{A})$ and $\mathrm{Rank}(\mathbf{A})$. $\mathbf{A}_{[x,y]}$ represents the element at the x_{th} row and the y_{th} column. Additionally, the positive semidefinite matrix is expressed $\mathbf{A} \succeq 0$. $\mathbb{R}^{n\times m}, \mathbb{C}^{n\times m}$ are the set of $n\times m$ real matrices and complex matrices. The special matrices $\mathbf{0}_{N\times N}$ and $\mathbf{I}_{N\times N}$ denote $N \times N$ the all-zero matrix and identity matrix.

II. End-to-end Communication Model and Problem Formulation

A. End-to-end Communication Model

The S-parameter is utilized to present the relationship (i.e., end-to-end communication model $\mathbf{H}_{\mathrm{E2E}}$) between the voltages of the transmitter (Tx) and receiver (Rx). Indeed, the S-parameter can describe any type of RF system with concise form, $\mathbf{b} = \mathbf{S}\mathbf{a}$, where $\mathbf{b}$ and $\mathbf{a}$ are the reflection and incident waves attached to the system. With the idea of the S-parameter, the RIS-assisted communication system can be seen as a huge N-port network. Then considering the load or source matching effects of all the end (i.e., Tx, Rx or RIS), the $\mathbf{H}_{\mathrm{E2E}}$ can be achieved by [24, section III]. Its specific form is

$$\mathbf{H}_{\mathrm{E2E}} = (\mathbf{\Gamma}_{R,L} + \mathbf{I})\,\mathbf{S}\mathbf{G}^{-1} \times \left(\mathbf{I} + (\mathbf{\Gamma}_S + \mathbf{I})\left(\mathbf{S}_{TT}(\mathbf{I} - \mathbf{\Gamma}_S\mathbf{S}_{TT})^{-1}\right)\right)^{-1}, \quad (1)$$

where $\mathbf{\Gamma}_{R,L}$ and $\mathbf{\Gamma}_S$ denote the reflection-coefficient matrices of the Rx load and the Tx source. Particularly, they are diagonal matrices, whose elements are the reflection coefficients of the units at the Rx and Tx. Moreover, $\mathbf{S}_{TT}$ is the S-parameter matrix of the Tx array. All the inverse operations can be guaranteed in the practical engineering design. Besides, $\mathbf{S}$ and $\mathbf{G}$ are presented as

$$\mathbf{S} = \begin{bmatrix} \mathbf{S}_{TT} & \mathbf{0} & \mathbf{0} \\ \mathbf{S}_{IT} & \mathbf{S}_{II} & \mathbf{0} \\ \mathbf{S}_{RT} & \mathbf{S}_{RI} & \mathbf{S}_{RR} \end{bmatrix}, \quad (2)$$

$$\mathbf{G} = \begin{bmatrix} \mathbf{I} - \mathbf{\Gamma}_S\mathbf{S}_{TT} & \mathbf{0} & \mathbf{0} \\ -\mathbf{\Theta}\mathbf{S}_{IT} & \mathbf{I} - \mathbf{\Theta}\mathbf{S}_{II} & \mathbf{0} \\ -\mathbf{\Gamma}_{R,L}\mathbf{S}_{RT} & -\mathbf{\Gamma}_{R,L}\mathbf{S}_{RI} & \mathbf{I} - \mathbf{\Gamma}_{R,L}\mathbf{S}_{RR} \end{bmatrix}. \quad (3)$$

The matrices similar to $\mathbf{S}_{AB}$, where $A, B \in \{T, R, I\}$, are the transmission matrices between the end A and end B. Accordingly, the dimension of the matrix is $N_A \times N_B$, where N_A and N_B are the numbers of units at the end A and end B. Moreover, the matrices with the form of $\mathbf{S}_{AA}$ denote the S-parameter matrices of the arrays in various ends. Specifically, $\mathbf{\Theta}$ is the reflection coefficient matrix of the RIS. It is worth mentioning that equations (2) and (3) are under the assumption without the $\mathbf{S}_{TI}$, $\mathbf{S}_{IR}$, and $\mathbf{S}_{TR}$ due to their negligible values [9]. Further, we can achieve (4), where $\mathbf{T} = \mathbf{I} - \mathbf{\Gamma}_{R,L}\mathbf{S}_{RR}$, by adopting the inverse of the block matrix.

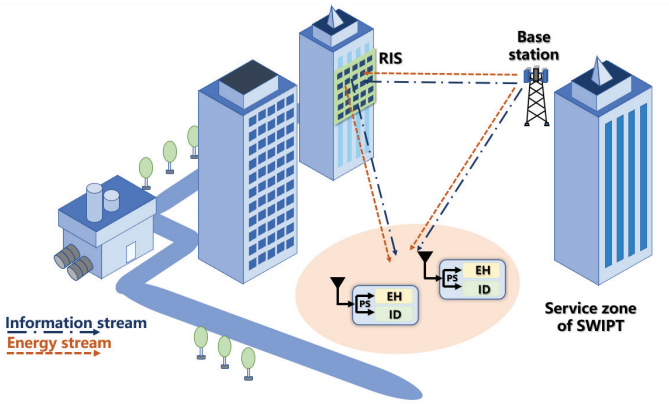

Fig. 1: The RIS-enhanced-SWIPT system.

Then, inserting (2) and (4) into (1), the end-to-end channel model is shown as

$$\mathbf{H}_{\mathrm{E2E}} = \mathbf{Q}\mathbf{S}_{RT}\mathbf{P} + \mathbf{Q}\mathbf{S}_{RI}(\mathbf{\Theta}^{-1} - \mathbf{S}_{II})^{-1}\mathbf{S}_{IT}\mathbf{P}, \quad (5)$$

in which, the shorthand notations are presented as $\mathbf{Q} = (\mathbf{\Gamma}_{R,L}+\mathbf{I})(\mathbf{I}-\mathbf{S}_{RR}\mathbf{\Gamma}_{R,L})^{-1}$ and $\mathbf{P} = (\mathbf{I}+\mathbf{S}_{TT})^{-1}$. Compared to the common-adopted cascaded channel model for the RIS-assisted network, (5) includes not only the transfer components $\mathbf{S}_{RT}$, $\mathbf{S}_{IT}$, and $\mathbf{S}_{RI}$, which contain the random transmission items, but also the main hardware features of all the ends. Particularly, the mismatching impacts and MC effects of the devices are described through the S-parameter matrices $\mathbf{S}_{AA}$ and reflection coefficient matrices. Indeed, $\mathbf{H}_{\mathrm{E2E}}$ brings a chance to analyze the system through the practical hardware. Furthermore, its generality makes it compatible with any type of antenna or reflection configuration.

B. problem Formulation

Relying on the model, this paper constructs a RIS-assisted SWIPT network with MISO downlink as in Fig. 1. There are $N_T > 1$ antennas at the Tx and the Rx adopts a single antenna. Besides, the RIS is introduced to enhance the transfer quality of the SWIPT. In this scenario, the load reflection coefficients of the RIS are assumed to be configured through the varactors

$$\mathbf{G}^{-1} = \begin{bmatrix} (\mathbf{I} - \mathbf{\Gamma}_S\mathbf{S}_{TT})^{-1} & \mathbf{0} & \mathbf{0} \\ (\mathbf{I} - \mathbf{\Theta}\mathbf{S}_{II})^{-1}\mathbf{\Theta}\mathbf{S}_{IT}(\mathbf{I} - \mathbf{\Gamma}_S\mathbf{S}_{TT})^{-1} & (\mathbf{I} - \mathbf{\Theta}\mathbf{S}_{II})^{-1} & \mathbf{0} \\ \mathbf{T}^{-1}\mathbf{\Gamma}_{R,L}(\mathbf{S}_{RT} + \mathbf{S}_{RI}(\mathbf{I} - \mathbf{\Theta}\mathbf{S}_{II})^{-1}\mathbf{\Theta}\mathbf{S}_{IT})(\mathbf{I} - \mathbf{\Gamma}_S\mathbf{S}_{TT})^{-1} & \mathbf{T}^{-1}\mathbf{\Gamma}_{R,L}\mathbf{S}_{RI}(\mathbf{I} - \mathbf{\Theta}\mathbf{S}_{II})^{-1} & \mathbf{T}^{-1} \end{bmatrix}. \quad (4)$$

[25], thus they have continuously adjustable levels. Particularly, the users have colocated forms with dual demands. For separating the ID and EH streams received by them, we utilize the PS scheme. Moreover, the set $\mathcal{N}_U = \{1, \ldots, N_U\}$ is adopted to include all the users. Then adding the active beamforming items, the received signal is presented by

$$y_i = \mathbf{h}_i(\mathbf{\Theta}) \left(\sum_{i=1}^{N_U} \mathbf{w}_i x_i \right) + n_i, \tag{6}$$

where $\mathbf{w}_i \in \mathbb{C}^{N_T \times 1}$ is the beamforming vector for the i^{th} user. In detail, x_i is the variable following Gaussian random distribution, namely, $x_i \sim \mathcal{CN}(0,1)$. Moreover, $n_i \sim \mathcal{CN}(0, \sigma_i^2)$ represents the noise of the antenna with the zero mean and σ_i^2 variance. Besides, $\mathbf{h}_i \in \mathbb{C}^{1 \times N_T}$ comes from

$$\mathbf{h}_i(\mathbf{\Theta}) = \mathbf{s}_{RT,i} + \mathbf{s}_{RI,i}(\mathbf{\Theta}^{-1} - \mathbf{S}_{II})^{-1}\mathbf{S}_{IT,i}, \tag{7}$$

in which we assume the matching conditions of the Tx antennas, Rx antennas, and Rx loads are perfect. Besides, the MC effects of the Tx array can be ignored owing to its sufficient element spacing. With the above assumptions, we can make $\mathbf{Q} = \mathbf{I}$ and $\mathbf{P} = \mathbf{I}$ in (5), thus (7) can be achieved.

Moreover, the PS-based user has the splitting ratios $0 < \rho_i < 1$ for the ID streams and $1 - \rho_i$ for the EH streams. Then we can define the signal for ID as

$$y_i = \sqrt{\rho_i} \left(\mathbf{h}_i(\mathbf{\Theta}) \left(\sum_{i=1}^{N_U} \mathbf{w}_i x_i \right) + n_i \right) + u_i, \tag{8}$$

where u_i denotes the signal processing noise with zero mean and δ_i^2 variance at the ID components. Particularly $u_i \sim \mathcal{CN}(0, \delta_i^2)$. With (8), we can further define the signal-to-interference plus noise ratio (SINR) of each user as

$$\varpi_i \left(\mathbf{w}_i, \rho_i, \mathbf{\Theta} \right) = \frac{\rho_i |\mathbf{h}_i(\mathbf{\Theta})\mathbf{w}_i|^2}{\rho_i \sum_{l \neq i}^{N_U} |\mathbf{h}_i(\mathbf{\Theta})\mathbf{w}_l|^2 + \rho_i \sigma_i^2 + \delta_i^2}. \tag{9}$$

Similarly, the received power is written as follows.

$$P_{\mathrm{RF},i} \left(\mathbf{w}_i, \rho_i, \mathbf{\Theta} \right) = (1 - \rho_i)\mathbf{h}_i(\mathbf{\Theta}) \left(\sum_{i=1}^{N_U} \mathbf{w}_i \mathbf{w}_i^H \right) \mathbf{h}_i(\mathbf{\Theta})^H. \tag{10}$$

Furthermore, (10) is the received RF power, which should be rectified to the DC power for supplying the electric equipment of the Rxs. During rectification, the non-linearity of diodes should be considered. Therefore, given the required DC power $P_{\mathrm{DC},i}^{(\mathrm{D})}$, we can achieve its corresponding RF power E_i by the following non-linear fitting model.

$$E_i(P_{\mathrm{DC},i}^{(\mathrm{D})}) = \varrho_i - \frac{1}{\kappa_i} \ln \left(\frac{P_{B,i} \left(1 + \exp(\kappa_i \varrho_i)\right)}{P_{\mathrm{DC},i}^{(\mathrm{D})} \exp(\kappa_i \varrho_i) + P_{B,i}} - 1 \right), \tag{11}$$

where ϱ_i and κ_i denote the parameters of the rectifying circuit. Moreover, $P_{B,i}$ represents the maximum DC power.

The sum rate of the users and the overall consumption of energy are both considered as vital items in this paper. In order to balance them, we introduce the EE indicator as

$$\mathrm{EE} \left(\mathbf{w}_i, \rho_i, \mathbf{\Theta} \right) = \frac{\sum_{i=1}^{N_U} R_i \left(\mathbf{w}_i, \rho_i, \mathbf{\Theta} \right)}{P \left(\mathbf{w}_i, \rho_i, \mathbf{\Theta} \right)}, \tag{12}$$

where rate is set as $R_i \left(\mathbf{w}_i, \rho_i, \mathbf{\Theta} \right) = \log_2(1 + \varpi_i \left(\mathbf{w}_i, \rho_i, \mathbf{\Theta} \right))$. Moreover, $P \left(\mathbf{w}_i, \rho_i, \mathbf{\Theta} \right)$ is the dissipated power of the whole system. Its specific expression can be written as follows.

$$P \left(\mathbf{w}_i, \rho_i, \mathbf{\Theta} \right) = \sum_{i=1}^{N_U} \|\mathbf{w}_i\|_2^2 + P_b + \xi \left(\sum_{i=1}^{N_U} R_i \left(\mathbf{w}_i, \rho_i, \mathbf{\Theta} \right) \right), \tag{13}$$

In the above equation, $\sum_{i=1}^{N_U} \|\mathbf{w}_i\|_2^2$ is the total transmitting power. $P_b = P_c + N_I P_I$ denotes the basic power consumption, where P_c and P_I are the energy dissipation of the front-end devices at the Tx and the RIS element. $\xi(\sum_{i=1}^{N_U} R_i \left(\mathbf{w}_i, \rho_i, \mathbf{\Theta} \right))$ is a rate-dependent item, which denotes the dissipation of the signal-processing energy. ξ represents the ratio of the power usage per unit data rate.

We then take into account an EE maximization problem based on the mentioned settings. Particularly, the form of the optimization problem is presented as the following $\mathbf{P}_0$.

$$\mathbf{P}_0 : \max_{\{\mathbf{w}_i, \rho_i, \mathbf{\Theta}\}} \mathrm{EE} \left(\mathbf{w}_i, \rho_i, \mathbf{\Theta} \right) \tag{14a}$$

$$\text{s.t.} \sum_{i=1}^{N_U} \|\mathbf{w}_i\|_2^2 \leq P_{\mathrm{Max}}, \tag{14b}$$

$$\varpi_i \left(\mathbf{w}_i, \rho_i, \mathbf{\Theta} \right) \geq 2^{R_i^{(\mathrm{D})}} - 1, \forall i, \tag{14c}$$

$$P_{\mathrm{RF},i} \left(\mathbf{w}_i, \rho_i, \mathbf{\Theta} \right) \geq E_i(P_{\mathrm{DC},i}^{(\mathrm{D})}), \forall i, \tag{14d}$$

$$0 < \rho_i < 1, \forall i, \tag{14e}$$

$$|\mathbf{\Theta}_{[n,n]}| \leq 1, \forall n. \tag{14f}$$

In (14b), P_{Max} is the maximal power constraint for the Tx. (14c) and (14d) are the guarantees of the user's QoS, respectively. As for (14c), the data-rate requirement of the user is denoted as $R_i^{(\mathrm{D})}$. (14d) is the power-supply demand. The range of the PS ratio is presented in (14e). Concerning the RIS, the reflection coefficients of the diagonal elements are constrained in (14f). Nevertheless, the problem $\mathbf{P}_0$ is a non-convex problem, which cannot be optimized directly. Specifically, the inverse form of the channel model (7) renders the problem more intractable.

III. Solution Approach

In this section, we propose the optimization scheme for handling the problem $\mathbf{P}_0$. In particular, the problem is broken down into a series of simplified problems by introducing the Neuman series approximation. Then the the inner AO approach is applied to resolve the subproblems based on different variables.

A. Neuman Series Approximation

The model adopted in this paper is derived from S-parameter analysis and has the inverse form, which adds complexity to the problem. For conducting the subsequent optimization, we first introduce the Neuman series approximation proposed in [26]. Particularly, we can add a variable $\mathbf{D}$ with initial fixed $\mathbf{\Theta}^{(0)}$ to replace the existed $\mathbf{\Theta}$ in (7).

$$\mathbf{h}_i(\mathbf{D}) = \mathbf{s}_{RT,i} + \mathbf{s}_{RI,i}(\mathbf{\Theta}^{(0)^{-1}} - \mathbf{S}_{II} + \mathbf{D})^{-1}\mathbf{S}_{IT,i}, \tag{15}$$

where $\mathbf{D}$ is presented as $\mathrm{diag}\left(\Delta_1, \cdots, \Delta_{N_I}\right)$. Furthermore, according to (15), we can make an equivalent transformation for the item $\mathcal{G}(\mathbf{D}) = (\boldsymbol{\Theta}^{(0)^{-1}} - \mathbf{S}_{II} + \mathbf{D})^{-1}$ as

$$\begin{aligned}&\mathcal{G}(\mathbf{D})\\&= \left[\mathbf{I} - \left(-(\boldsymbol{\Theta}^{(0)^{-1}} - \mathbf{S}_{II})^{-1}\mathbf{D}\right)\right]^{-1}\left(\boldsymbol{\Theta}^{(0)^{-1}} - \mathbf{S}_{II}\right)^{-1} \quad (16)\\&= \sum_{n=0}^{+\infty}\left(-\left(\boldsymbol{\Theta}^{(0)^{-1}} - \mathbf{S}_{II}\right)^{-1}\mathbf{D}\right)^{n}\left(\boldsymbol{\Theta}^{(0)^{-1}} - \mathbf{S}_{II}\right)^{-1}, \quad (17)\end{aligned}$$

Theorem 1: When the norms of the elements in the diagonal matrix $\mathbf{D}$ are sufficiently small, the equation (17) can be approximated as follows.

$$\mathcal{G}(\mathbf{D}) \approx \left(\mathbf{I} - (\boldsymbol{\Theta}^{(0)^{-1}} - \mathbf{S}_{II})^{-1}\mathbf{D}\right)\left(\boldsymbol{\Theta}^{(0)^{-1}} - \mathbf{S}_{II}\right)^{-1}. \quad (18)$$

Proof: See Appendix A.

In (18), $(\boldsymbol{\Theta}^{(0)^{-1}} - \mathbf{S}_{II})^{-1}$ is fixed, thus the inverse item in (15) is transformed into a solvable form. However, since there is a strict constraint for ensuring accuracy, the optimization for $\mathbf{D}$ cannot be achieved in one step. Indeed, we can construct an iteration-based scheme with variable $\mathbf{D}^{(j)}$, where the superscript j denotes the j^{th} turn for the problem $\mathbf{P}_0$.

Through (18), we can further approximate the j^{th} channel model during the optimization.

$$\mathbf{h}_i^{(j)}(\mathbf{D}^{(j)}) \approx \mathbf{g}_i^{(j)} + \mathbf{z}_i^{(j)}\mathbf{D}^{(j)}\mathbf{E}_i^{(j)}, \quad (19)$$

where the introduced shorthand notations can be presented as $\mathbf{g}_i^{(j)} = \mathbf{s}_{RT,i} + \mathbf{s}_{RI,i}(\boldsymbol{\Theta}^{(j-1)^{-1}} - \mathbf{S}_{II})^{-1}\mathbf{S}_{IT,i}$, $\mathbf{z}_i^{(j)} = -\mathbf{s}_{RI,i}(\boldsymbol{\Theta}^{(j-1)^{-1}} - \mathbf{S}_{II})^{-1}$, and $\mathbf{E}_i^{(j)} = (\boldsymbol{\Theta}^{(j-1)^{-1}} - \mathbf{S}_{II})^{-1}\mathbf{S}_{IT,i}$. After each solution, the optimized $\mathbf{D}^{(j)^*}$ will be passed into $\boldsymbol{\Theta}^{(j)^{-1}} = \boldsymbol{\Theta}^{(j-1)^{-1}} + \mathbf{D}^{(j)^*}$ for building the new $\boldsymbol{\Theta}^{(j)^{-1}}$. Furthermore, the problem of the j^{th} iteration can be written as

$$\begin{aligned}\mathbf{P}_1^{(j)}: &\max_{\left\{\mathbf{w}_i^{(j)}, \rho_i^{(j)}, \mathbf{D}^{(j)}\right\}} \mathrm{EE}\left(\mathbf{w}_i^{(j)}, \rho_i^{(j)}, \mathbf{D}^{(j)}\right) && (20a)\\ \text{s.t. }&, \varpi_i\left(\mathbf{w}_i^{(j)}, \rho_i^{(j)}, \mathbf{D}^{(j)}\right) \geq 2^{R_i^{(\mathrm{D})}} - 1, \forall i, && (20b)\\ &P_{\mathrm{RF},i}\left(\mathbf{w}_i^{(j)}, \rho_i^{(j)}, \mathbf{D}^{(j)}\right) \geq E_i(P_{\mathrm{DC},i}^{(\mathrm{D})}), \forall i, && (20c)\\ &\left|(\boldsymbol{\Theta}^{(j-1)^{-1}} + \mathbf{D}^{(j)})^{-1}_{[n,n]}\right| \leqslant 1, \forall n, && (20d)\\ &|\Delta_n^{(j)}| \leqslant \zeta, \forall n. && (20e)\\ &(14b), (14e)\end{aligned}$$

Although the problem $\mathbf{P}_1^{(j)}$ has a similar structure to the problem $\mathbf{P}_0$, the constraints (20d) and (20e) have significant difference owing to the introduced approximation. Particularly, the accuracy guarantee of (20e) comes from (18). Moreover, (20d) makes sure that the physical limit $|\boldsymbol{\Theta}^{(j)}{}_{[n,n]}| \leqslant 1, \forall n$, is satisfied. However, the term $(\boldsymbol{\Theta}^{(j-1)^{-1}} + \mathbf{D}^{(j)})^{-1}$ still has an inverse form. As $\boldsymbol{\Theta}^{(j-1)^{-1}}$ and $\mathbf{D}^{(j)}$ both are diagonal matrices, we can achieve equivalent constraint without the inverse for (20d) as follows.

$$\left|(\boldsymbol{\Theta}^{(j-1)^{-1}} + \mathbf{D}^{(j)})_{[n,n]}\right| \geq 1, \forall n, \quad (21)$$

Algorithm 1 Proposed scheme based on the AO scheme and the Neuman series approximation

Initialize: ε_{total}, ε_{AO};
1: Set $j = 1$, $k = 1$, $\boldsymbol{\Theta}^{(0)}$, $\mathbf{D}^{(1)}(0) = \mathbf{0}$, $B_{total} > \varepsilon_{total}$, $\mathrm{EE}^{(0)} = 0$;
2: **while** $B_{total} \geq \varepsilon_{total}$ **do**
3: Using (19) for obtaining the updated channel model;
4: Set $\mathbf{D}^{(j)^*}(k-1) = \mathbf{0}$, $B_{AO} > \varepsilon_{AO}$, $\mathrm{EE}\,(0) = 0$;
5: **while** $B_{AO} \geq \varepsilon_{AO}$ **do**
6: Solving the subproblem of $\left\{\mathbf{w}_i^{(j)}(k), \rho_i^{(j)}(k)\right\}$;
7: Solving the subproblem of $\left\{\mathbf{D}^{(j)}(k)\right\}$;
8: Set $B_{AO} = \mathrm{EE}\,(k) - \mathrm{EE}\,(k-1)$;
9: Update $k = k + 1$;
10: **end while**
11: Return $\left\{\mathbf{w}_i^{(j)^*}(k), \rho_i^{(j)^*}(k), \mathbf{D}^{(j)^*}(k)\right\}$;
12: Set $B_{total} = \mathrm{EE}^{(j)} - \mathrm{EE}^{(j-1)}$;
13: update $k = 1$, $j = j + 1$;
14: **end while**
Output: the optimal $\{\mathbf{w}_i^*, \rho_i^*, \mathbf{D}^*\}$

Even so, $\mathbf{P}_1^{(j)}$ is still complicated to address due to the fractional objective and the non-convex constraints. For resolving them, we first adopt the AO scheme to decouple the variables.

B. AO Scheme

According to the inner part of Algorithm 1, we deconstruct the problem $\mathbf{P}_1^{(j)}$ into two parts. These two subproblems will be tackled iteratively until the stop condition is met.

1) Optimization of $\left\{\mathbf{w}_i^{(j)}, \rho_i^{(j)}\right\}$: We first solve the variables $\mathbf{w}_i^{(j)}(k)$ and $\rho_i^{(j)}(k)$ with the fixed $\mathbf{D}^{(j)^*}(k-1)$ in the k^{th} turn of the AO scheme. For simplicity, we omit the iteration notation (k) in the remaining content. Before optimizing, we introduce the semi-definite relaxation (SDR) approach for the beamforming vector $\mathbf{w}_i^{(j)}$. In detail, we denote $\mathbf{W}_i^{(j)} = \mathbf{w}_i^{(j)}\mathbf{w}_i^{(j)^H}$, while introducing $\mathbf{W}_i^{(j)} \succeq 0$, $\mathrm{rank}(\mathbf{W}_i^{(j)}) = 1$. As regards the channel model (19), we then define $\hat{\mathbf{H}}_i^{(j)} = \mathbf{h}_i^{(j)^H}\mathbf{h}_i^{(j)}$. Further, we can rewrite the problem as following $\mathbf{P}_{2\text{-A}}$.

$$\begin{aligned}\mathbf{P}_{2\text{-A}}: &\max_{\left\{\mathbf{w}_i^{(j)}, \rho_i^{(j)}\right\}} \frac{\sum_{i=1}^{N_U} R_i\left(\mathbf{W}_i^{(j)}, \rho_i^{(j)}\right)}{P\left(\mathbf{W}_i^{(j)}, \rho_i^{(j)}\right)} && (22a)\\ \text{s.t. }&\sum_{i=1}^{N_U}\mathrm{Tr}(\mathbf{W}_i^{(j)}) \leq P_{\mathrm{Max}}, && (22b)\\ &\frac{\mathrm{Tr}(\hat{\mathbf{H}}_i^{(j)}\mathbf{W}_i^{(j)})}{2^{R_i^{(\mathrm{D})}} - 1} - \sum_{l\neq i}^{N_U}\mathrm{Tr}(\hat{\mathbf{H}}_i^{(j)}\mathbf{W}_l^{(j)}) \geq \sigma_i^2 + \frac{\delta_i^2}{\rho_i^{(j)}}, \forall i, && (22c)\\ &\mathrm{Tr}(\hat{\mathbf{H}}_i^{(j)}\sum_{i=1}^{N_U}\mathbf{W}_i^{(j)}) \geq \frac{E_i(P_{\mathrm{DC},i}^{(\mathrm{D})})}{1 - \rho_i^{(j)}}, \forall i, && (22d)\\ &0 < \rho_i^{(j)} < 1, \forall i. && (22e)\\ &\mathbf{W}_i^{(j)} \succeq 0, \mathrm{rank}(\mathbf{W}_i^{(j)}) = 1, \forall i, && (22f)\end{aligned}$$

where the trace form of the matrix is used in place of the power-related components, thus the problem is easier to solve. Particularly, the reformed data rate and the utilized energy in (22a) can be presented as

$$R_i\left(\mathbf{W}_i^{(j)},\rho_i^{(j)}\right) = \log_2\left(1+\frac{\mathrm{Tr}(\hat{\mathbf{H}}_i^{(j)}\mathbf{W}_i^{(j)})}{\sum_{l\neq i}^{N_U}\mathrm{Tr}(\hat{\mathbf{H}}_i^{(j)}\mathbf{W}_l^{(j)})+\sigma_i^2+\frac{\delta_i^2}{\rho_i^{(j)}}}\right), \quad (23)$$

$$P\left(\mathbf{W}_i^{(j)},\rho_i^{(j)}\right) = \sum_{i=1}^{N_U}\mathrm{Tr}(\mathbf{W}_i^{(j)})+P_b+\xi\left(\sum_{i=1}^{N_U}R_i\left(\mathbf{W}_i^{(j)},\rho_i^{(j)}\right)\right). \quad (24)$$

However, the problem $\mathbf{P}_{2\text{-A}}$ still cannot be addressed directly due to the objective (22a). Before utilizing the approach of fractional optimization, we introduce several slack variables and matched constraints.

$$\mathbf{P}_{2\text{-B}}: \max_{\left\{\begin{smallmatrix}\mathbf{w}_i^{(j)},\rho_i^{(j)},\\ \Lambda_i^{(j)}\end{smallmatrix}\right\}} \frac{\sum_{i=1}^{N_U}u_i^{(j)}}{\sum_{i=1}^{N_U}\mathrm{Tr}(\mathbf{W}_i^{(j)})+P_b+\xi(\sum_{i=1}^{N_U}u_i^{(j)})} \quad (25a)$$

$$\text{s.t. } \mathrm{Tr}(\hat{\mathbf{H}}_i^{(j)}\mathbf{W}_i^{(j)}) \geq t_i^{(j)}o_i^{(j)},\forall i, \quad (25b)$$

$$t_i^{(j)} \geq 2^{(u_i^{(j)})}-1,\forall i, \quad (25c)$$

$$\sum_{l\neq i}^{N_U}\mathrm{Tr}(\hat{\mathbf{H}}_i^{(j)}\mathbf{W}_l^{(j)})+\sigma_i^2+\frac{\delta_i^2}{\rho_i^{(j)}} \leq o_i^{(j)},\forall i, \quad (25d)$$

(22b)-(22f).

where $\Lambda_i^{(j)} \triangleq \{u_i^{(j)},t_i^{(j)},o_i^{(j)}\}$ is the combination of the slack variables. Moreover, (25c) and (25d) are the convex constraints, whereas (25b) still is a non-convex constraint. According to the INCA approach proposed in [27] and [28], we make an equivalent conversion for the bilinear term $t_i^{(j)}o_i^{(j)} = \frac{1}{2}\left((t_i^{(j)}+{o_i^{(j)}}^2)-{t_i^{(j)}}^2-{o_i^{(j)}}^2\right)$. Furthermore, the Taylor expansion can be introduced to find the lower bound of the terms ${t_i^{(j)}}^2$ and ${o_i^{(j)}}^2$.

$${t_i^{(j)}}^2 \geq {\bar{t}_i^{(j)}}^2+2\bar{t}_i^{(j)}(t_i^{(j)}-\bar{t}_i^{(j)}), \quad (26)$$

$${o_i^{(j)}}^2 \geq {\bar{o}_i^{(j)}}^2+2\bar{o}_i^{(j)}(o_i^{(j)}-\bar{o}_i^{(j)}). \quad (27)$$

Through them, the upper bound of (25b) can be reformed as

$$\begin{aligned}\mathrm{Tr}(\hat{\mathbf{H}}_i^{(j)}\mathbf{W}_i^{(j)}) \geq& \frac{1}{2}(t_i^{(j)}+o_i^{(j)})^2 \\ &-\left[\frac{1}{2}{\bar{t}_i^{(j)}}^2+\bar{t}_i^{(j)}(t_i^{(j)}-\bar{t}_i^{(j)})\right] \\ &-\left[\frac{1}{2}{\bar{o}_i^{(j)}}^2+\bar{o}_i^{(j)}(o_i^{(j)}-\bar{o}_i^{(j)})\right],\end{aligned} \quad (28)$$

where $\bar{t}_i^{(j)}$ and $\bar{o}_i^{(j)}$ denote the feasible values of $t_i^{(j)}$ and $o_i^{(j)}$. Replacing (25b) with (28), the modified problem will be invoked several times for updating $\bar{t}_i^{(j)}$ and $\bar{o}_i^{(j)}$ until the convergence condition is satisfied. This is the idea of the INCA scheme. Even so, the remaining objective formulation is still intractable during the optimization. Nevertheless, it now has the concave/convex form, which can be utilized with the Dinkelbach's Algorithm.

Algorithm 2 The Dinkelbach's algorithm based on the INCA scheme

Initialize: $\epsilon = 0$;
1: **Repeat**
2: **Repeat**
3: Achieve $t_i^{(j)^*}$ and $o_i^{(j)^*}$ by optimizing $\mathbf{P}_{2-\text{C}}$;
4: Update $\bar{t}_i^{(j)}$ and $\bar{o}_i^{(j)}$ with $t_i^{(j)^*}$ and $o_i^{(j)^*}$;
5: **Until** The values of EE meet the convergence condition.
6: Update $\epsilon^* = \frac{\sum_{i=1}^{N_U}R_i\left(\mathbf{W}_i^{(j)^*},\rho_i^{(j)^*}\right)}{P\left(\mathbf{W}_i^{(j)^*},\rho_i^{(j)^*}\right)}$;
7: Reset the stop condition for the INCA scheme.
8: **Until** $\Upsilon\left(\mathbf{W}_i^{(j)},u_i^{(j)}\right)$ meet the stop condition.
9: Obtain $\mathbf{w}_i^{(j)^*}$ from the eigenvector of $\mathbf{W}_i^{(j)^*}$, when the rank-one condition is met. Otherwise, Gaussian randomization should be introduced [30].
Output: the optimal $\mathbf{w}_i^{(j)^*}$ and $\rho_i^{(j)^*}$.

Lemma 1: When ϵ^* is the unique zero, the objective equation (25a) can be replaced by the subtraction form as

$$\begin{aligned}&\Upsilon\left(\mathbf{W}_i^{(j)},u_i^{(j)}\right) \\ &= \sum_{i=1}^{N_U}u_i^{(j)}-\epsilon\left(\sum_{i=1}^{N_U}\mathrm{Tr}(\mathbf{W}_i^{(j)})+P_b+\xi\left(\sum_{i=1}^{N_U}u_i^{(j)}\right)\right).\end{aligned} \quad (29)$$

Proof: The proof was presented in [29], we omit the detailed process here. Then, the problem based on the INCA and Dinkelbach's scheme is shown as

$$\mathbf{P}_{2\text{-C}}: \max_{\left\{\begin{smallmatrix}\mathbf{w}_i^{(j)},\rho_i^{(j)},\\ \Lambda_i^{(j)}\end{smallmatrix}\right\}} \Upsilon\left(\mathbf{W}_i^{(j)},u_i^{(j)}\right)$$
$$\text{s.t. (28), (25c), (25d), (22b)-(22f).}$$

We can further drop the rank-one constraint in (22f) to let $\mathbf{P}_{2\text{-C}}$ become a convex problem, which can be tackled by the conventional approaches. The detailed recovery process, satisfying the rank-one constraint, from $\mathbf{W}_i^{(j)^*}$ to $\mathbf{w}_i^{(j)^*}$ can adopt the decomposition of the eigenvector or Gaussian randomization [30]. The specific solution procedure based on the above schemes is presented in Algorithm 2. Particularly, steps 2-5 represent the INCA scheme and the outer steps are the details of Dinkelbach's algorithm. For simplicity, we omit the iteration notations.

2) Optimization of $\{\mathbf{D}^{(j)}\}$*:* Then we can tackle the problem related to the variable $\{\mathbf{D}^{(j)}\}$ with the optimal $\{\mathbf{w}_i^{(j)^*},\rho_i^{(j)^*}\}$ from the above solution. Similarly, the SDR approach is also introduced for reforming the problem. According to (19), we can define the notations as

$$\mathbf{B}_{il}^{(j)} = \begin{bmatrix}\mathbf{e}_{il}^{(j)}\mathbf{e}_{il}^{(j)^H} & \mathbf{e}_{il}^{(j)}\hat{g}^{(j)^H} \\ \mathbf{e}_{il}^{(j)^H}\hat{g}^{(j)} & 0\end{bmatrix}, \quad \hat{\mathbf{q}}^{(j)} = \begin{bmatrix}\mathbf{q}^{(j)} \\ 1\end{bmatrix}, \quad (30)$$

where $\hat{g}_{il}^{(j)} = \mathbf{g}_i^{(j)}\mathbf{w}_l^{(j)^*}$, $\mathbf{e}_{il}^{(j)} = \text{diag}(\mathbf{z}_i^{(j)})\mathbf{E}_i^{(j)}\mathbf{w}_l^{(j)^*}$, and $\mathbf{q}^{(j)} \triangleq [\Delta_1^{(j)}; \cdots; \Delta_{N_I}^{(j)}]$. Then we denote $\hat{\mathbf{Q}}^{(j)} = \hat{\mathbf{q}}^{(j)^H}\hat{\mathbf{q}}^{(j)}$ with the additional constraint $\hat{\mathbf{Q}}^{(j)} \succeq 0$ and $\text{rank}(\hat{\mathbf{Q}}^{(j)}) = 1$. Based on the definitions of the matrices, the rate term and the power term can be presented in (31) and (32).

$$P\left(\hat{\mathbf{Q}}^{(j)}\right) = \sum_{i=1}^{N_U}\left\|\mathbf{w}_i^{(j)^*}\right\|_2^2 + P_b + \xi\left(\sum_{i=1}^{N_U} R_i\left(\hat{\mathbf{Q}}^{(j)}\right)\right). \tag{32}$$

The specific expression of the subproblem for $\hat{\mathbf{Q}}^{(j)}$ is shown in (33a). Among them, (33e) comes from (20e), which refers to the accuracy of the approximation. Moreover, (33d) is the reflection coefficient constraint, which is based on the equivalent equation (21) of (20d).

Proposition 1: After deploying the SDR approach for $\mathbf{D}^{(j)}$, the constraint (21) can be rewritten as (33d).

Proof: See Appendix B.

Dropping the rank-one constraint, the problem $\mathbf{P}_{3\text{-A}}$ still has an intricate objective (33a). Similarly, the formulation may turn out into a solvable form by using the structure of Algorithm 2 with the Dinkelbach's algorithm and the INCA scheme. The expression of the reformed problem can be written as in $\mathbf{P}_{3\text{-B}}$.

$$\mathbf{P}_{3\text{-B}}: \max_{\left\{\hat{\mathbf{Q}}^{(j)}, \Psi_i^{(j)}\right\}} \Xi(z_i^{(j)}) \tag{34a}$$

$$\text{s.t. } v_i^{(j)} \geq 2^{(z_i^{(j)})} - 1, \tag{34b}$$

$$\text{Tr}(\mathbf{B}_{ii}^{(j)}\hat{\mathbf{Q}}^{(j)}) + |\hat{g}_{ii}^{(j)}|^2 \geq \mathcal{M}(v_i^{(j)}, w_i^{(j)}), \tag{34c}$$

$$\sum_{l\neq i}^{N_U}\left(\text{Tr}(\mathbf{B}_{il}^{(j)}\hat{\mathbf{Q}}^{(j)}) + |\hat{g}_{il}^{(j)}|^2\right) + \sigma_i^2 + \frac{\delta_i^2}{\rho_i^{(j)}} \leq w_i^{(j)}, \tag{34d}$$

(33b)-(33f).

The problem inserts some variables mainly for deconstructing the rate term of (33a). In the problem, $\Psi_i^{(j)} \triangleq \{z_i^{(j)}, v_i^{(j)}, w_i^{(j)}\}$. Moreover, the objective formulation $\Xi(\hat{\mathbf{Q}}^{(j)}, z_i^{(j)})$ and the lower bound item $\mathcal{M}(v_i^{(j)}, w_i^{(j)})$ of (34a) and (34c) can be shown as

$$\begin{aligned}&\Xi(z_i^{(j)})\\ &= \sum_{i=1}^{N_U} z_i^{(j)} - \tau\left(\sum_{i=1}^{N_U}\left\|\mathbf{w}_i^{(j)^*}\right\|_2^2 + P_b + \xi(\sum_{i=1}^{N_U} z_i^{(j)})\right),\end{aligned} \tag{35}$$

$$\begin{aligned}&\mathcal{M}(v_i^{(j)}, w_i^{(j)})\\ &= \frac{1}{2}(v_i^{(j)} + w_i^{(j)})^2 - \left[\frac{1}{2}\bar{v}_i^{(j)^2} + \bar{v}_i^{(j)}(v_i^{(j)} - \bar{v}_i^{(j)})\right]\\ &- \left[\frac{1}{2}\bar{w}_i^{(j)^2} + \bar{w}_i^{(j)}(w_i^{(j)} - \bar{w}_i^{(j)})\right].\end{aligned} \tag{36}$$

Since the whole solving procedures are nearly identical to the solution for the previous subproblem, we won't go into the details here. After handling the iterations of Dinkelbach's algorithm and the INCA scheme, $\hat{\mathbf{Q}}^{(j)^*}$ also can utilize the decomposition approach from Algorithm 2 to recover the $\mathbf{D}^{(j)^*}$ for the next AO solution.

The overall structure of the proposed optimization scheme for the problem $\mathbf{P}_0$ has been described completely. Interestingly, when the MC and the mismatching effects of RIS are ignored, namely $\mathbf{S}_{II} = \mathbf{0}$, the problem can be tackled through the inner AO approach without Neuman series approximation. Nevertheless, this may bring optimization deviation in practical situations, which will be shown in the next section.

IV. Simulation Results

In this section, we first design a practical RIS for extracting its key parameters. Particularly, its S-parameter matrix, which includes the MC and the mismatching effects, is then applied

$$R_i\left(\hat{\mathbf{Q}}^{(j)}\right) = \log_2\left(1 + \frac{\text{Tr}(\mathbf{B}_{ii}^{(j)}\hat{\mathbf{Q}}^{(j)}) + |\hat{g}_{ii}^{(j)}|^2}{\sum_{l\neq i}^{N_U}\left(\text{Tr}(\mathbf{B}_{il}^{(j)}\hat{\mathbf{Q}}^{(j)}) + |\hat{g}_{il}^{(j)}|^2\right) + \sigma_i^2 + \frac{\delta_i^2}{\rho_i^{(j)}}}\right). \tag{31}$$

$$\mathbf{P}_{3\text{-A}}: \max_{\{\hat{\mathbf{Q}}^{(j)}\}} \frac{\sum_{i=1}^{N_U} R_i\left(\hat{\mathbf{Q}}^{(j)}\right)}{P\left(\hat{\mathbf{Q}}^{(j)}\right)} \tag{33a}$$

$$\text{s.t. } \frac{\text{Tr}(\mathbf{B}_{ii}^{(j)}\hat{\mathbf{Q}}^{(j)}) + |\hat{g}_{ii}^{(j)}|^2}{2^{R_i^{(\text{D})}} - 1} \geq \sum_{l\neq i}^{N_U}(\text{Tr}(\mathbf{B}_{il}^{(j)}\hat{\mathbf{Q}}^{(j)}) + |\hat{g}_{il}^{(j)}|^2) + \sigma_i^2 + \frac{\delta_i^2}{\rho_i^{(j)}}, \forall i, \tag{33b}$$

$$\text{Tr}\left(\mathbf{B}_{ii}^{(j)}\hat{\mathbf{Q}}^{(j)}\right) + |\hat{g}_{ii}^{(j)}|^2 \geq \frac{E_i(P_{\text{DC},i}^{(\text{D})})}{1 - \rho_i^{(j)}}, \forall i, \tag{33c}$$

$$\hat{\mathbf{Q}}_{[n,n]}^{(j)} + \hat{\mathbf{Q}}_{[n,N_I+1]}^{(j)}\hat{\mathbf{\Theta}}_{[N_I+1,n]}^{(j-1)} + \hat{\mathbf{\Theta}}_{[N_I+1,n]}^{(j-1)^H}(\hat{\mathbf{Q}}_{[N_I+1,n]}^{(j)} + \hat{\mathbf{\Theta}}_{[N_I+1,n]}^{(j-1)}) \geq 1, \forall n, \hat{\mathbf{Q}}_{[N_I+1,N_I+1]}^{(j)} \geq 1, \tag{33d}$$

$$\hat{\mathbf{Q}}_{[n,n]}^{(j)} \leqslant \zeta^2, \forall n, \tag{33e}$$

$$\hat{\mathbf{Q}}^{(j)} \succeq 0, \text{rank}(\hat{\mathbf{Q}}^{(j)}) = 1. \tag{33f}$$

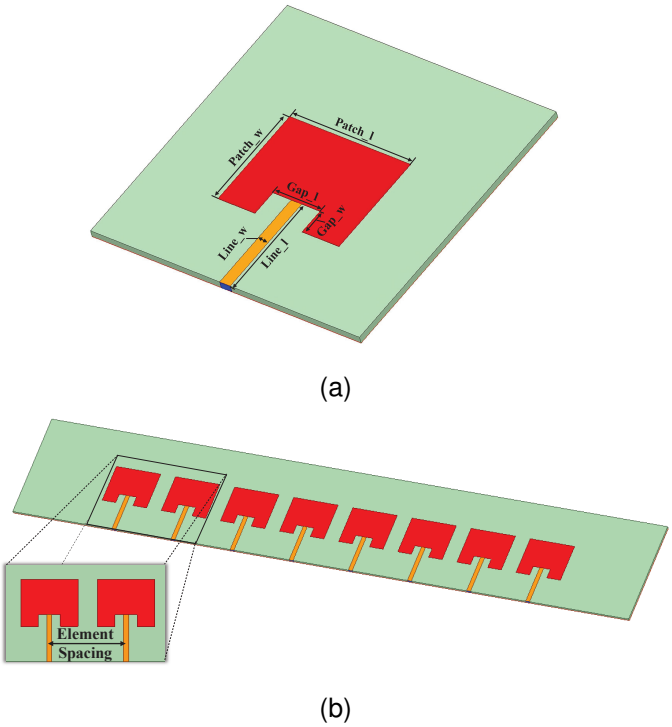

Fig. 2: (a) The element design of RIS. (b) A linear-array design of RIS.

to the problem solution. In detail, the simulations about the impacts of QoS demands (i.e., the requirements of the power supply and the data rate) and the transmitting-power budgets are conducted under some typical cases to reveal the effects of taking into account physical features. Moreover, the research about the configuration of the RIS is also introduced to reflect the importance of the hardware design. During the performance comparisons, the effectiveness of the proposed solution strategy is presented.

A. Simulation of RIS

Within the context of this paper, the element with the patch form, which is similar to the design in [31], is utilized as a representative example to construct the RIS. It is worth mentioning that the end-to-end model proposed in (5) isn't limited to this configuration. On the contrary, it is highly compatible with any type of entity. Moreover, the specific form of the created reflection element, operating at 2.45GHz, is presented in Fig. 2 (a). The top side of the element includes the transmission line and reflection patch. In detail, the tail end of the line can be connected to the varactors, which brings the configured $\mathbf{\Theta}$, for reflecting incident waves. Moreover, the back side is the copper layer for prevention of the wave leakage. All the physical parameters are presented in Table I.

On the basis of this element, we further design an 8-element-linear-array RIS for the 2-dimension simulation scenario in Fig. 2 (b). When adjusting the element spacing d_I between the units, $\mathbf{S}_{II}$ will be varied accordingly. Particularly, we utilize $\mathrm{S}(1,1)$ and $\mathrm{S}(2,1)$, which denote the matching and the MC terms, to represent these changes in the diagonal elements and the off-diagonal elements of $\mathbf{S}_{II}$, respectively. The relationships between the element spacings and the S parameters can be found in Fig. 3. As the spacing shrinks, the original matching condition at $d_I = 61.2mm$, which is equal to $\lambda/2$ at 2.45GHz, will be distorted in Fig. 3 (a). Besides, the isolation between the elements is also broken in Fig. 3 (b). It means that the closer spacing brings the stronger MC effects. Indeed, these impacts may also affect the entire network in addition to the RIS. In the next subsection, we will research these effects from the system perspective.

TABLE I: STRUCTURE PARAMETERS

Parameter	Value/mm	Parameter	Value/mm
Patch_l	36	Gap_w	7.3
Patch_w	29.2	Line_l	29.8
Gap_l	16	Line_w	3.15

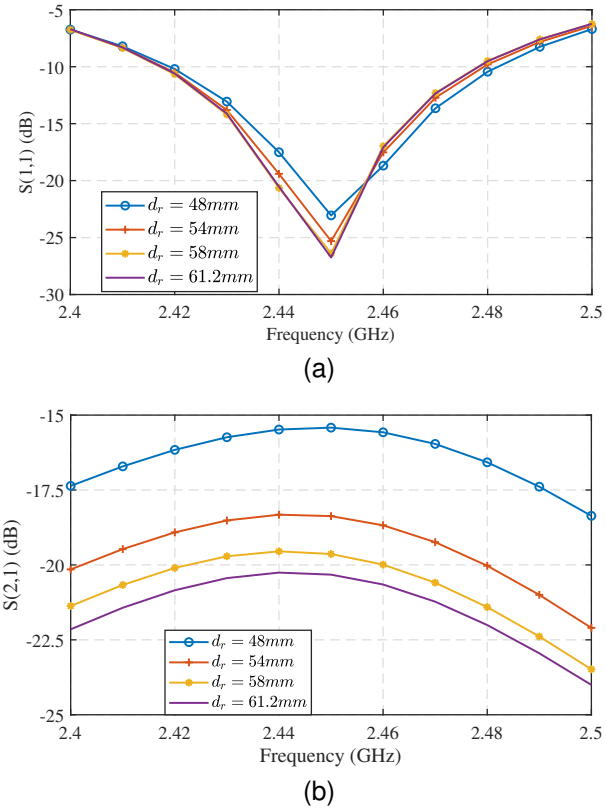

Fig. 3: (a) $\mathrm{S}(1,1)$ under distinct element spacing. (b) $\mathrm{S}(2,1)$ under distinct element spacing.

B. Numerical Results

In this part, we import the S-parameter matrix of the designed RIS into the EE optimization through the end-to-end channel model (7). Particularly, the simulations mainly relate to the QoS requirements and the RIS configurations. As the mismatching effects are negligible in Fig. 3 (a), we only study the influences of MC effects in this paper. Specifically, all these results are conducted under the situations of no MC,

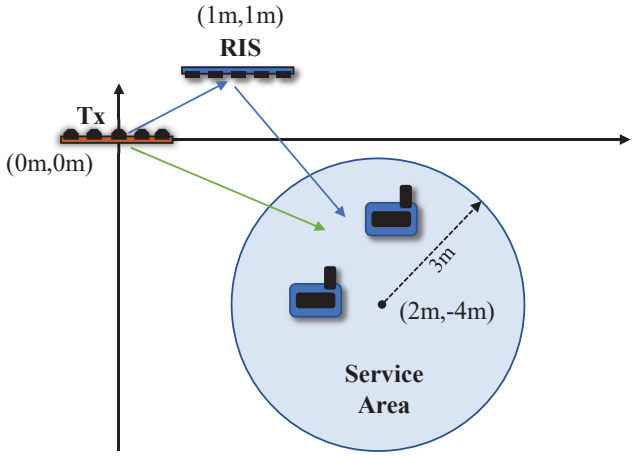

Fig. 4: The 2-dimension application scenario for the RIS-assisted SWIPT network.

MC-awareness, MC-unawareness, no RIS, and unoptimized RIS. The findings of the comparative analyses will prove the importance of MC effects in the system analysis.

We consider the 2-dimension application scenario for the RIS-assisted SWIPT network at 2.45GHz. In detail, the Tx, which is equipped with an 8-element array, is located at (0m,0m). Moreover, its element spacing is set as $\lambda/2$. The configuration of RIS is mentioned in the last subsection and its center is set at (1m,1m). To maintain the compactness, we make the default spacing between the RIS element $48mm$, which is less than $\lambda/2$. Besides, the two users are generated within the service area. The region is constrained into a circle with (2m,-4m) center and 3m radius. The simplified scene diagram with the above descriptions is presented in Fig. 4.

As for the transfer matrices $\mathbf{S}_{IT}$, $\mathbf{s}_{RT}$, and $\mathbf{s}_{RI}$, we utilize the Rician channel as in [24]. their expressions are

$$\mathbf{S}_{IT} = \sqrt{L_{IT}}\left(\sqrt{\frac{\mathcal{K}}{1+\mathcal{K}}}\mathbf{H}_{IT}^{\text{LoS}} + \sqrt{\frac{1}{1+\mathcal{K}}}\mathbf{H}_{IT}^{\text{NLoS}}\right), \quad (37)$$

$$\mathbf{s}_{RT} = \sqrt{L_{RT}}\left(\sqrt{\frac{\mathcal{K}}{1+\mathcal{K}}}\mathbf{h}_{RT}^{\text{LoS}} + \sqrt{\frac{1}{1+\mathcal{K}}}\mathbf{h}_{RT}^{\text{NLoS}}\right), \quad (38)$$

$$\mathbf{s}_{RI} = \sqrt{L_{RI}}\left(\sqrt{\frac{\mathcal{K}}{1+\mathcal{K}}}\mathbf{h}_{RI}^{\text{LoS}} + \sqrt{\frac{1}{1+\mathcal{K}}}\mathbf{h}_{RI}^{\text{NLoS}}\right), \quad (39)$$

where $\mathcal{K}$ denote the Rician factor. Pathloss L_{AB} can be calculated as $L_{AB} = (\frac{\lambda}{4\pi})^2\left(\frac{d_{AB}}{D_0}\right)^{-\alpha_{AB}}$ with the reference distance $D_0 = 1m$. Besides, α_{AB} is the loss coefficient. d_{AB} denotes the distance between the end A and the end B. It can further be calculated from their coordinate positions. Particularly, the parameters are chosen as $\alpha_{IT} = 2.2$, $\alpha_{RI} = 2.5$, $\alpha_{RT} = 3$, and $\mathcal{K} = 10$dB. As for the LoS term, $\mathbf{H}_{RT}^{\text{LoS}} = \mathbf{a}_{\text{RIS}}^T\mathbf{a}_{\text{Tx}}$, $\mathbf{h}_{IT}^{\text{LoS}} = \mathbf{a}_{\text{Tx}}$, and $\mathbf{h}_{IR}^{\text{LoS}} = \mathbf{a}_{\text{RIS}}$. The equation of the array response is presented as follows.

$$\mathbf{a}_N(\theta) = \left[1, e^{-j2\pi\frac{d}{\lambda}\sin\theta}, \ldots, e^{-j2\pi(N-1)\frac{d}{\lambda}\sin\theta}\right], \quad (40)$$

where $N = \{N_I, N_T\}$ of the RIS and Tx and θ denotes the angle of departure (AoD) or the angle of arrival (AoA).

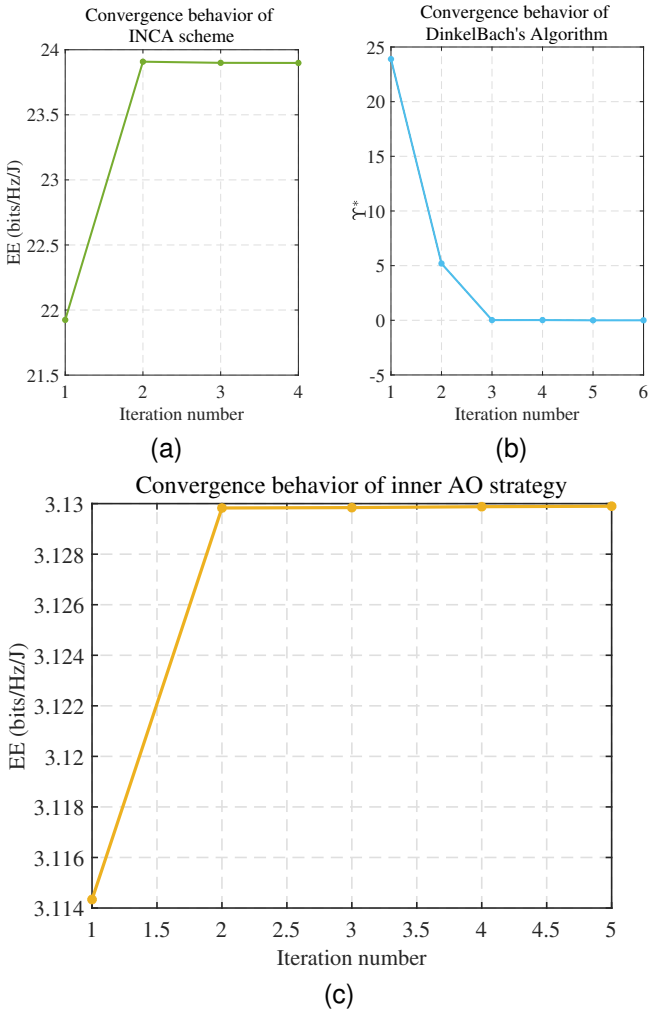

Fig. 5: (a) Convergence behavior of INCA scheme. (b) Convergence behavior of Dinkelbach's algorithm. (b) Convergence behavior of inner AO strategy.

Additionally, $d \in \{d_I, d_T\}$ represents the element spacings. Moreover, all the non-LoS items follow the Rayleigh fading model. The above parameters are traced from [32] and [33].

The minimal requirement of EH $P_{\text{DC},i}^{(\text{D})} = 1.3\mu\text{W}, \forall i$ and the rate demand is set as $R_i^{(\text{D})} = 1\text{bit/s/Hz}, \forall i$. As for the power budget, it is constrained as $P_{\text{Max}} = 9\text{W}$. Besides, the power consumptions of the front-end devices and the RIS is configured as $P_c = 1$ W and $P_I = 10$ mW. The power-dissipation ratio of the signal processing is $\xi = 0.01$. Furthermore, the two types of the noise power $\sigma_i^2 = -100\text{dBm}, \forall i$ and $\delta_i^2 = -90\text{dBm}, \forall i$. These parameters can be referenced to [32]. Moreover, we utilize the HSMS2860 diode to constitute the rectifying circuit. Then, the relevant circuit parameters for the non-linear fitting equation (11) are generated as $\varrho_i = 5.61$, $\kappa_i = 0.242$, and $P_B = 8.577$. The default settings for the above parameters won't be modified unless they are the indicators chosen to be analyzed.

1) Convergence Behaviors: In this part, the convergence behaviors are shown in Fig. 5 for demonstrating the effective-

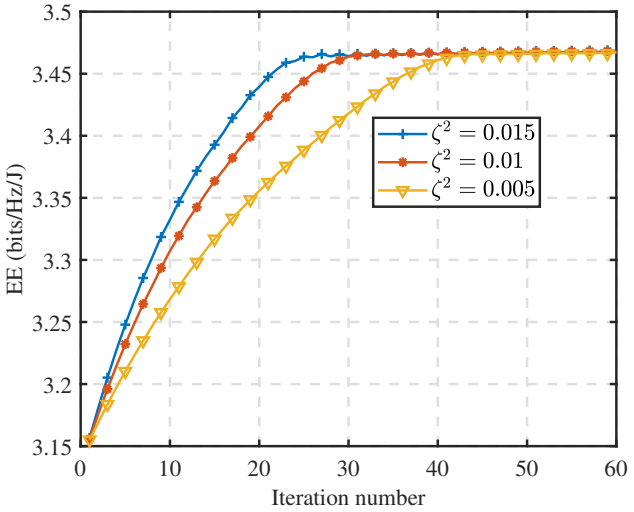

Fig. 6: The convergence behavior of total optimization structure based on the Neuman series approximation.

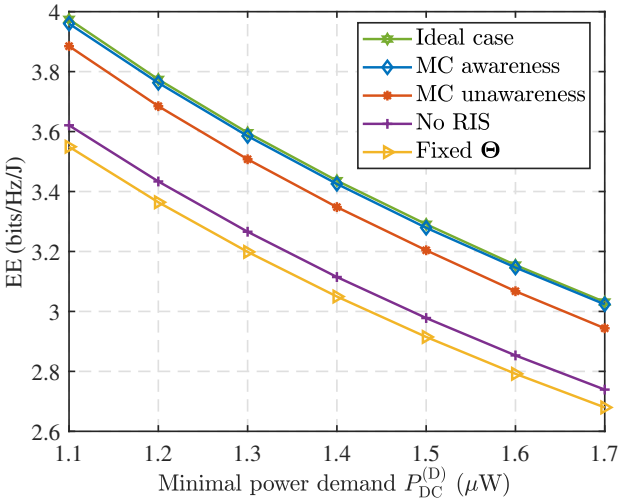

Fig. 7: The EE performance versus the demand of the minimal rectified power $P_{\mathrm{DC}}^{(\mathrm{D})}$.

ness of the simulations. Particularly, the proposed optimization structure is constructed on the Neuman series approximation. In detail, the inner part of the AO scheme further consists of the INCA approach and Dinkelbach's algorithm. During the solution, all these schemes should converge to a steady condition. As in Fig. 5, we can find that the objective values of the schemes come near to stable numbers within three iterations, which verifies their convergence. Indeed, the AO scheme is enough for situations without the effects of the MC and the mismatching, because the inverse item is nonexistent. However, it is just a part of the solution under the practical circumstance. The convergence behavior of the proposed total structure for the MC-awareness case is shown in Fig. 6. In particular, we can see that the distinct indicators ζ^2 presented in (33e), the constraint about the accuracy guarantee, cause various speeds of convergence. Additionally, the larger ζ^2 has the faster convergence rate, while the curve is unsmooth. This phenomenon comes from the loss of the approximation accuracy. After weighing the accuracy and the speed, we choose $\zeta^2 = 0.01$ for the subsequent simulations.

2) The analyses of QoS requirements and power budget: In this part, we conduct a series of comparisons under the distinct QoS requirements and power budget. First, we study the influence of the minimal power demand on the EE indicator in Fig. 7. Particularly, the ideal case assumes that the MC effect is nonexistent at the RIS. We set it as the benchmark for the other simulation results. Furthermore, the MC awareness, which is a practical case, consists of results from the optimization under the consideration of the MC effect. Then, the MC unawareness represents inserting the optimal variables from the ideal case to the practical condition. The performance difference between the MC-awareness case and the MC-unawareness case is apparent. The reason is that the optimization deviation occurs when the MC effect is ignored. What's more, the above three cases have better performance than the No-RIS case and the unoptimized-RIS case. It illustrates that the RIS indeed gives performance enhancement to the SWIPT system by improving the transmission quality. In either case, the EE indicators decrease with the intense demand for minimal rectified power, since the power dissipation is increasing. In detail, the denominator of (12) keeps getting larger and the numerator stays at the same level, so the EE values are smaller.

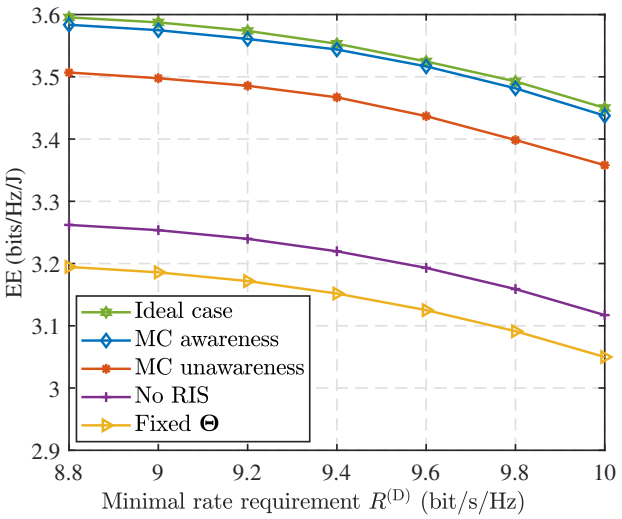

Fig. 8: The EE performance versus the requirement of the minimal rate $R^{(\mathrm{D})}$.

We further research the impacts of the minimal rate requirement. As in Fig. 8, the performance differences between the various cases are consistent with Fig. 7. Particularly, the results of MC awareness still outperform other cases except for the ideal case. Although the performance levels are distinct, they all have decreasing tendencies with the increase of $R^{(\mathrm{D})}$. This phenomenon comes from two aspects. First, the user with the better channel quality will achieve more power supply because of the sum rate of the EE, when the rate requirements are

This article has been accepted for publication in IEEE Internet of Things Journal. This is the author's version which has not been fully edited and content may change prior to final publication. Citation information: DOI 10.1109/JIOT.2023.3347623

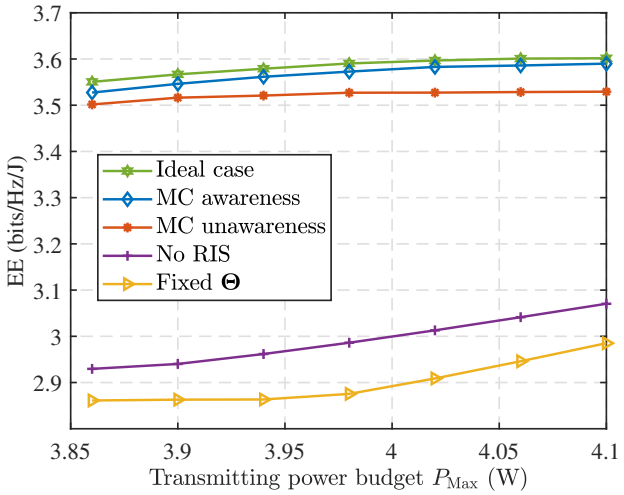

Fig. 9: The EE performance versus the transmitting power budget P_{Max}.

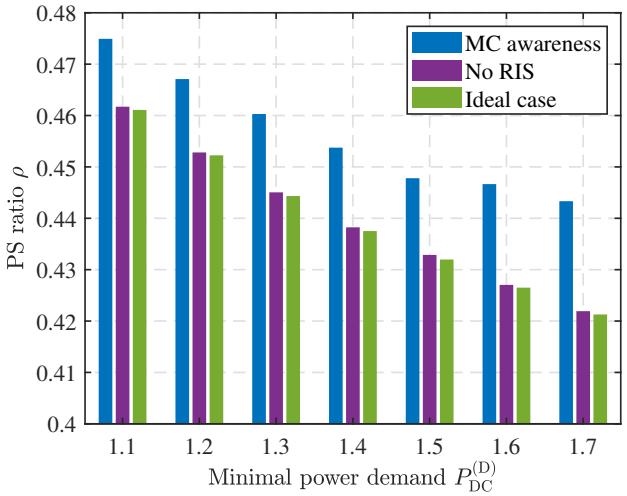

Fig. 10: The PS ratio ρ versus the demand of the minimal rectified power $P_{\text{DC}}^{(\text{D})}$.

not intense. It means that the system can get more economic EE improvement by giving the extra energy costs to the user, which has a larger space for rate enhancement. Nevertheless, the disposable power will be less as the rate requirements of all users increase simultaneously. At this time, the user with a relatively worse channel needs more energy to satisfy the minimum threshold. Indeed, the power consumption turns out to be costly. All these facts demonstrate that the enhancement of the sum rate cannot catch up with the substantially increased power costs, which causes EE to decrease. The second reason is that the higher demand for the rate also brings more signal-processing requirements. As in (13), this also needs additional power dissipation, which is followed by the worse EE.

Then we research the effects of the distinct transmitting budgets in Fig. 9. Since the performance gaps among the comparative cases keep in line with the above simulations, we omit the descriptions of the reasons. Furthermore, it can be found that the EE values increase in all cases. However, their variation trends have slight differences. The growth speeds of the EE are decreasing gradually in the situations of the ideal case, the MC awareness, and the MC unawareness. This phenomenon results from that the sum rate is enhanced and the input of the P_{Max} will get into a stalemate in the post-growth period. In other words, the power cannot support the improvement of the sum rate economically. Besides, the power increase also causes the interference items $\sum_{l\neq i}^{N_U} |\mathbf{h}_i(\boldsymbol{\Theta})\mathbf{w}_k|$ in (9) to become larger, which further shrinks the EE values. However, this stalemate does not occur in the cases of the No RIS and the unoptimized RIS, since their EE levels are lower and there is still plenty of room for growth.

Finally, we are curious about the PS ratios of users in typical situations. The minimal power requirement is utilized as varied factors in Fig. 10. We select the ideal case, the MC awareness, and the No RIS to constitute the comparative simulations. As the power demand enhances, the PS ratio ρ decreases in all the cases. This implies that $(1-\rho)$, which denotes the portion for the EH as in (10), is increasing. Interestingly, the ratio $(1-\rho)$

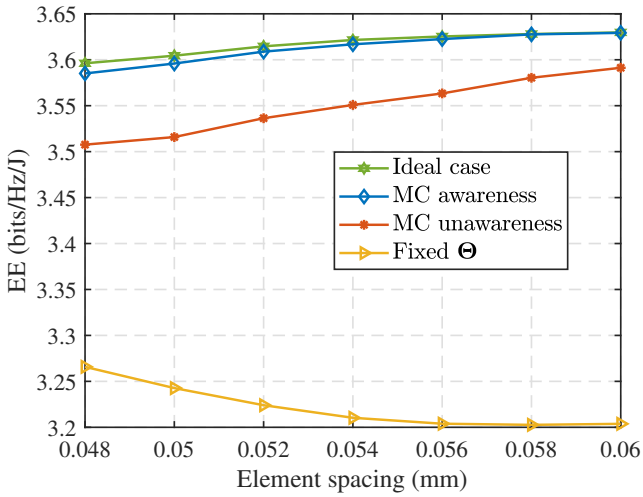

Fig. 11: The EE performance versus the element spacing.

of the MC awareness is lower than the ratios of the other two cases. This means the MC-awareness case can distribute more energy to the data rate. Even so, owing to the existence of the strong MC effects, its EE performance is slightly worse than the performance of the ideal case as in Fig. 7.

The conducted simulations indicate that our proposed optimization scheme for MC awareness is effective. Moreover, it also demonstrates that the MC effects indeed influence the EE and ignoring its existence will lead to non-negligible optimization deviation.

3) The research about the RIS configuration: The levels of the MC effects directly rely on the element spacings. When the distance is closer, more waves will couple to the adjacent units. However, the RIS always adopts the closely-coupled array to shrink its area, which is brought from the large number of elements. The specific reason is that nearly-passive RIS can achieve better performance only by configuring more elements. For analyzing the influence of compact structure,

the related studies are presented in Fig. 11. When the distance increases from $48mm$ to $60mm$, which is close to $\lambda/2$, the EE performance is enhanced in the ideal case, MC-awareness case, and MC-unawareness case. In particular, it demonstrates the fact that the larger element spacings produce the higher performance in this range. Meanwhile, the performance gaps among these cases become smaller. This phenomenon comes from the reason that MC effects play an unimportant role in the optimization under situations with larger distances. However, the consequences, which are caused by optimization deviation of the MC-unawareness situation, always exist and are worth considering. Besides, the performance of the unoptimized RIS is worse in the large-spacing situations, since the fixed $\mathbf{\Theta}$ makes the reflection waves deviate from the intended direction in this scenario.

V. Conclusion

An end-to-end RIS-assisted communication model, which is based on the S-parameter analysis, was proposed to reveal the key physical features of the ends (i.e., Tx, Rx, and RIS) in this paper. Especially, the MC effect of the closely-coupled RIS array was considered as a prominent factor. Through the model, an EE maximization problem was introduced to balance the sum rate and the power dissipation. To solve the issue, we adopted the iteration scheme relying on the approximation approach of the Neuman series. With this idea, the inverse item of the transfer model can be tackled effectively. In each inner iteration, the variables (i.e., active beamforming vector, PS radio, and reflection coefficients of RIS) were optimized by the AO strategy. Further, the separated two subproblems were reformed through the SDR. Then the approach based on the INCA and Dinkelbach's algorithm was utilized to turn them into a solvable form. In the simulations, we first analyzed the relationship between the convergence speed and the approximation accuracy. Then several studies about the various QoS requirements and transmitting-power levels were conducted. All the results demonstrates that the MC effect is an indispensable factor during the optimization and ignorance of its influence caused the non-negligible performance gap. Moreover, the analysis related to the element spacing of the RIS also presented that the MC effect should be considered carefully. In order to expand the end-to-end model for future research, we will examine other effects brought about by hardware factors (e.g., the nonlinearity of the power amplifier and the element arrangement of the RIS). Moreover, the accurate modeling for the rectifier will also be examined for making the research of the RIS-aided-SWIPT network more practical.

Appendix
Proof of the Theorem 1

The approximation brings the gap between (16) and (18). To ensure accuracy, we should find the upper bound of the difference. Referring to [26, Theorem 4.20], the gap between the sum of first k terms in (17) and (18) satisfies the following inequality.

$$\left\|\sum_{n=0}^{k}\left(-\left(\mathbf{\Theta^{(0)}}^{-1}-\mathbf{S}_{II}\right)^{-1}\mathbf{D}\right)^{n}-\left(\left(\mathbf{\Theta^{(0)}}^{-1}-\mathbf{S}_{II}\right)^{-1}\mathbf{D}+\mathbf{I}\right)^{-1}\right\|\leq\frac{\left\|-\left(\mathbf{\Theta^{(0)}}^{-1}-\mathbf{S}_{II}\right)^{-1}\mathbf{D}\right\|^{k+1}}{1-\left\|-\left(\mathbf{\Theta^{(0)}}^{-1}-\mathbf{S}_{II}\right)^{-1}\mathbf{D}\right\|},\tag{41}$$

where we remove the same fixed term $\left(\mathbf{\Theta^{(0)}}^{-1}-\mathbf{S}_{II}\right)^{-1}$ from the equations. Through (41), the right-hand term should be controlled at a low level considering the accuracy. Particularly, the condition is presented as

$$\left\|-\left(\mathbf{\Theta^{(0)}}^{-1}-\mathbf{S}_{II}\right)^{-1}\mathbf{D}\right\|\ll 1\tag{42}$$

Furthermore, we can achieve

$$\left\|-\left(\mathbf{\Theta^{(0)}}^{-1}-\mathbf{S}_{II}\right)^{-1}\mathbf{D}\right\|\leq\left\|-\left(\mathbf{\Theta^{(0)}}^{-1}-\mathbf{S}_{II}\right)^{-1}\right\|\|\mathbf{D}\|.\tag{43}$$

Since the term $\left(\mathbf{\Theta^{(0)}}^{-1}-\mathbf{S}_{II}\right)^{-1}$ is fixed, we now only need to keep $\|\mathbf{D}\|$ is small enough. This can be satisfied by setting the norms of elements in $\mathbf{D}$. Specifically, the expression can be found in the constraint (20e). Therefore, Theorem 1 is proved.

Appendix
Proof of the Proposition 1

According to (21), it can define the matrix $\mathbf{K}(\mathbf{D}^{(j)})$ as

$$\mathbf{K}(\mathbf{D}^{(j)})=\mathbf{\Theta}^{(j-1)^{-1}}+\mathbf{D}^{(j)}.\tag{44}$$

Moreover, $\hat{\mathbf{\Theta}}^{(j-1)}$ can be shown as

$$\hat{\mathbf{\Theta}}^{(j-1)}=\begin{bmatrix}1&\dots&0&\mathbf{\Theta}_{[1,1]}^{(j-1)^{-1}}\\ \vdots&\ddots&\vdots&\vdots\\ 0&\dots&1&\mathbf{\Theta}_{[N_I,N_I]}^{(j-1)^{-1}}\end{bmatrix},\tag{45}$$

where $\hat{\mathbf{\Theta}}^{(j-1)}_{[1:N_I,1:N_I]}$ is the identity matrix with dimension $N_I\times N_I$. Moreover, the elements of $\hat{\mathbf{\Theta}}^{(j-1)}_{[1:N_I,N_I+1]}$ are the diagonal elements of $\mathbf{\Theta}^{(j-1)^{-1}}$.

Based on the expression for $\hat{\mathbf{q}}^{(j)}$ in (30), we can get

$$\mathbf{k}(\hat{\mathbf{q}}^{(j)})=\hat{\mathbf{\Theta}}^{(j-1)}\hat{\mathbf{q}}^{(j)},\tag{46}$$

where $\mathbf{k}(\hat{\mathbf{q}}^{(j)})$ is the vector containing the diagonal elements of $\mathbf{K}(\mathbf{D}^{(j)})$. With the settings, we can rewrite the constraint (21) as the following inequation.

$$\begin{aligned}&\left(\mathbf{k}(\hat{\mathbf{q}}^{(j)})\mathbf{k}(\hat{\mathbf{q}}^{(j)})^{H}\right)_{[n,n]}\\&=\left(\hat{\mathbf{\Theta}}^{(j-1)}\hat{\mathbf{Q}}^{(j)}\hat{\mathbf{\Theta}}^{(j-1)^{H}}\right)_{[n,n]}\geq 1,\forall n,\end{aligned}\tag{47}$$

Further, the constraint (33d) can be achieved from the expansion for (47).

REFERENCES

[1] W. Shi, W. Xu, X. You, C. Zhao, and K. Wei, "Intelligent reflection enabling technologies for integrated and green internet-of-everything beyond 5G: Communication, sensing, and security," *IEEE Wirel. Commun.*, vol. 30, no. 2, pp. 147–154, 2023.

[2] R. Lyu, W. Cheng, B. Shen, Z. Ren, and H. Zhang, "OAM-SWIPT for IoE-driven 6G," *IEEE Commun. Mag.*, vol. 60, no. 3, pp. 19–25, 2022.

[3] Y. Zhao, B. Clerckx, and Z. Feng, "IRS-aided SWIPT: Joint waveform, active and passive beamforming design under nonlinear harvester model," *IEEE Trans. Commun.*, vol. 70, no. 2, pp. 1345–1359, 2022.

[4] S. Zargari, A. Khalili, Q. Wu, M. Robat Mili, and D. W. K. Ng, "Max-min fair energy-efficient beamforming design for intelligent reflecting surface-aided SWIPT systems with non-linear energy harvesting model," *IEEE Trans. Veh. Technol.*, vol. 70, no. 6, pp. 5848–5864, 2021.

[5] P. Lu, C. Song, and K. M. Huang, "A two-port multipolarization rectenna with orthogonal hybrid coupler for simultaneous wireless information and power transfer (SWIPT)," *IEEE Trans. Antennas Propag.*, vol. 68, no. 10, pp. 6893–6905, 2020.

[6] M. C. Ilter, R. Wichman, M. Säily, and J. Hämäläinen, "Information harvesting for far-field wireless power transfer," *IEEE Internet of Things Mag.*, vol. 5, no. 2, pp. 127–132, 2022.

[7] M. Noor-A-Rahim, F. Firyaguna, J. John, M. O. Khyam, D. Pesch, E. Armstrong, H. Claussen, and H. V. Poor, "Toward industry 5.0: Intelligent reflecting surface in smart manufacturing," *IEEE Commun. Mag.*, vol. 60, no. 10, pp. 72–78, 2022.

[8] A. Abrardo, D. Dardari, M. Di Renzo, and X. Qian, "MIMO interference channels assisted by reconfigurable intelligent surfaces: Mutual coupling aware sum-rate optimization based on a mutual impedance channel model," *IEEE Wireless Commun. Lett.*, vol. 10, no. 12, pp. 2624–2628, 2021.

[9] M. Morris and M. Jensen, "Network model for MIMO systems with coupled antennas and noisy amplifiers," *IEEE Trans. Antennas Propag.*, vol. 53, no. 1, pp. 545–552, 2005.

[10] S. Saab, A. Mezghani, and R. W. Heath, "Optimizing the mutual information of frequency-selective multi-port antenna arrays in the presence of mutual coupling," *IEEE Trans. Commun.*, vol. 70, no. 3, pp. 2072–2084, 2022.

[11] T. Wang, W. Han, Z. Zhong, J. Pang, G. Zhou, S. Wang, and Q. Li, "Electromagnetic-compliant channel modeling and performance evaluation for holographic MIMO," in *Proc. IEEE Globecom Workshops (GC Wkshps)*, 2022, pp. 747–752.

[12] H. Li, W. Cai, Y. Liu, M. Li, Q. Liu, and Q. Wu, "Intelligent reflecting surface enhanced wideband MIMO-OFDM communications: From practical model to reflection optimization," *IEEE Trans. Commun.*, vol. 69, no. 7, pp. 4807–4820, 2021.

[13] X. Cheng, Y. Lin, W. Shi, J. Li, C. Pan, F. Shu, Y. Wu, and J. Wang, "Joint optimization for RIS-assisted wireless communications: From physical and electromagnetic perspectives," *IEEE Trans. Commun.*, vol. 70, no. 1, pp. 606–620, 2022.

[14] G. Gradoni and M. Di Renzo, "End-to-end mutual coupling aware communication model for reconfigurable intelligent surfaces: An electromagnetic-compliant approach based on mutual impedances," *IEEE Wireless Commun. Lett.*, vol. 10, no. 5, pp. 938–942, 2021.

[15] Z. Mao, W. Wang, Q. Xia, C. Zhong, X. Pan, and Z. Ye, "Element-grouping intelligent reflecting surface: Electromagnetic-compliant model and geometry-based optimization," *IEEE Trans. Wireless Commun.*, vol. 21, no. 7, pp. 5362–5376, 2022.

[16] D. Badheka, J. Sapis, S. R. Khosravirad, and H. Viswanathan, "Accurate modeling of intelligent reflecting surface for communication systems," *IEEE Trans. Wireless Commun.*, vol. 22, no. 9, pp. 5871–5883, 2023.

[17] A. S. Parihar, P. Swami, V. Bhatia, and Z. Ding, "Performance analysis of SWIPT enabled cooperative-NOMA in heterogeneous networks using carrier sensing," *IEEE Trans. Veh. Technol.*, vol. 70, no. 10, pp. 10 646–10 656, 2021.

[18] S. Xu, Y. Du, J. Liu, and J. Li, "Intelligent reflecting surface based backscatter communication for data offloading," *IEEE Trans. Commun.*, vol. 70, no. 6, pp. 4211–4221, 2022.

[19] S. K. Singh, K. Agrawal, K. Singh, A. Bansal, C.-P. Li, and Z. Ding, "On the performance of laser-powered UAV-assisted SWIPT enabled multiuser communication network with hybrid noma," *IEEE Trans. Commun.*, vol. 70, no. 6, pp. 3912–3929, 2022.

[20] C. Pan, H. Ren, K. Wang, M. Elkashlan, A. Nallanathan, J. Wang, and L. Hanzo, "Intelligent reflecting surface aided MIMO broadcasting for simultaneous wireless information and power transfer," *IEEE J. Sel. Areas Commun.*, vol. 38, no. 8, pp. 1719–1734, 2020.

[21] Q. Wu and R. Zhang, "Joint active and passive beamforming optimization for intelligent reflecting surface assisted SWIPT under QoS constraints," *IEEE J. Sel. Areas Commun.*, vol. 38, no. 8, pp. 1735–1748, 2020.

[22] Y. Tang, G. Ma, H. Xie, J. Xu, and X. Han, "Joint transmit and reflective beamforming design for IRS-assisted multiuser MISO SWIPT systems," in *Proc. IEEE Int. Conf. Commun. (ICC), Jun. 2020*, pp. 1–6.

[23] Y. Zhao, B. Clerckx, and Z. Feng, "IRS-aided SWIPT: Joint waveform, active and passive beamforming design under nonlinear harvester model," *IEEE Trans. Commun.*, vol. 70, no. 2, pp. 1345–1359, 2022.

[24] S. Shen, B. Clerckx, and R. Murch, "Modeling and architecture design of reconfigurable intelligent surfaces using scattering parameter network analysis," *IEEE Trans. Wireless Commun.*, vol. 21, no. 2, pp. 1229–1243, 2022.

[25] R. Fara, P. Ratajczak, D.-T. Phan-Huy, A. Ourir, M. Di Renzo, and J. De Rosny, "A prototype of reconfigurable intelligent surface with continuous control of the reflection phase," *IEEE Wirel. Commun.*, vol. 29, no. 1, pp. 70–77, 2022.

[26] G. W. Stewart, *Matrix algorithms: volume 1: basic decompositions*. SIAM, 1998.

[27] P. Song, G. Scutari, F. Facchinei, and L. Lampariello, "D3M: Distributed multi-cell multigroup multicasting," in *Proc. IEEE Int. Conf. Acoust. Speech. Signal. Process. (ICASSP)*, 2016, pp. 3741–3745.

[28] G. Scutari, F. Facchinei, and L. Lampariello, "Parallel and distributed methods for constrained nonconvex optimization—part I: Theory," *IEEE Trans. Signal Process.*, vol. 65, no. 8, pp. 1929–1944, 2017.

[29] W. Dinkelbach, "On nonlinear fractional programming," *Manage. Sci.*, vol. 13, no. 7, pp. 492–498, 1967.

[30] Y. Lu, K. Xiong, P. Fan, Z. Zhong, and K. B. Letaief, "Robust transmit beamforming with artificial redundant signals for secure SWIPT system under non-linear EH model," *IEEE Trans. Wireless Commun.*, vol. 17, no. 4, pp. 2218–2232, 2018.

[31] G. C. Trichopoulos, P. Theofanopoulos, B. Kashyap, A. Shekhawat, A. Modi, T. Osman, S. Kumar, A. Sengar, A. Chang, and A. Alkhateeb, "Design and evaluation of reconfigurable intelligent surfaces in real-world environment," *IEEE Open J. Commun. Soc.*, vol. 3, pp. 462–474, 2022.

[32] E. Boshkovska, D. W. K. Ng, L. Dai, and R. Schober, "Power-efficient and secure WPCNs with hardware impairments and non-linear EH circuit," *IEEE Trans. Commun.*, vol. 66, no. 6, pp. 2642–2657, 2018.

[33] Z. Li, W. Chen, Q. Wu, H. Cao, K. Wang, and J. Li, "Robust beamforming design and time allocation for IRS-assisted wireless powered communication networks," *IEEE Trans. Commun.*, vol. 70, no. 4, pp. 2838–2852, 2022.